Dalton Transactions

ROYAL SOCIETY OF CHEMISTRY

PAPER

View Article Online
View Journal | View Issue

Cite this: *Dalton Trans.*, 2025, **54**, 1896

Selective hydroxylation of benzene to phenol *via* $Cu^{II}(\mu\text{-}O^{\bullet})Cu^{II}$ intermediate using a nonsymmetric dicopper catalyst†

Qin-Qin Hu,[a] Qi-Fa Chen,[a] Hong-Tao Zhang,*[a] Jia-Yi Chen,*[b] Rong-Zhen Liao[b] and Ming-Tian Zhang*[a]

Received 14th October 2024,
Accepted 4th December 2024

DOI: 10.1039/d4dt02872d

rsc.li/dalton

The one-step oxidation of benzene to phenol represents a significant and promising advancement in modern industries focused on the production of high-value-added chemical products. Nevertheless, challenges persist in achieving sufficient catalytic selectivity and preventing over-oxidation. Inspired by copper enzymes, we present a nonsymmetric dicopper complex ($[Cu^{II}_2(TPMAN)(\mu\text{-}OH)(H_2O)]^{3+}$, **1**) for the selective oxidation of benzene to phenol. Utilizing H_2O_2 as the oxidant, complex **1** demonstrates remarkable catalytic activity (a TON of 14 000 within 29 hours) and selectivity exceeding 97%, comparable to the finest homogeneous catalyst derived from first-row transition metals. It is noteworthy that the significant substituent effect, alongside a negligible kinetic isotope effect (KIE = 1.05), radical trapping experiments, and an inconsistent standard selectivity test of the $^{\bullet}OH$ radicals, all contradict the conventional Fenton mechanism and rebound pathway. Theoretical investigations indicate that the active $Cu^{II}(\mu\text{-}O^{\bullet})Cu^{II}\text{–}OH$ species generated through the cleavage of the O–O bond in the $Cu^{II}(\mu\text{-}1,1\text{-}OOH)Cu^{I}$ intermediate facilitates the hydroxylation of benzene *via* an electrophilic attack mechanism. The nonsymmetric coordination geometry is crucial in activating H_2O_2 and in the process of O–O bond cleavage.

Introduction

Phenol is a vital chemical extensively utilized in the manufacturing of plastics, phenolic resins, pharmaceuticals, disinfectants, and various other products.[1–3] Currently, the industrial synthesis of phenol predominantly relies on the three-step cumene process, which necessitates harsh reaction conditions and yields a mere 5% overall yield, accompanied by the equimolar production of acetone.[4,5] Consequently, the one-step hydroxylation of benzene to phenol using inexpensive oxidants such as oxygen or hydrogen peroxide has emerged as a promising alternative approach, gathering substantial interest.[6–10] However, this process faces two primary challenges: the activation of the phenylic C–H bond, which possesses a high bond dissociation energy of 113 kcal mol^{-1}, and the prevention of over-oxidation of the resulting phenol.

Significant advancements have been made in the development of heterogeneous materials[11–19] and homogeneous molecular catalysts[20–39] that facilitate this one-step phenol production. Nonetheless, these approaches remain distant from achieving large-scale industrial viability due to inadequate phenol yields and selectivity. To enhance the design of more efficient catalysts, extensive research has focused on elucidating the mechanism underlying aromatic hydroxylation, leading to the proposal of several reaction pathways. Notably, one mechanism suggests direct activation of the C–H bond by hydroxyl ($^{\bullet}OH$) or hydroperoxyl ($^{\bullet}OOH$) radicals produced *via* the Fenton-type reaction.[40–44] Alternative pathways include an electrophilic aromatic substitution pathway and a rebound pathway mediated by highly energetic metal–oxygen species, such as $Fe^{IV}{=}O$ species found in cytochrome-P_{450}.[45–50] Systematic investigations into molecular catalysts have revealed that the ligand denticity plays a crucial role in modulating the reaction activity and mechanism.[51,52] For instance, mononuclear iron complexes, featuring tridentate N3 ligands, preferentially follow a hydroxyl radical pathway due to the instability of the iron–oxygen intermediate, thereby resulting in lower selectivity.[53] In contrast, tetradentate N4 coordinated iron catalysts facilitate heterolytic cleavage of the O–O bond in the Fe^{III}–OOH species, aided by a free coordination site, ultimately yielding more reactive $Fe^{V}{=}O$ intermediates that enhance both yield and selectivity.[54] However, pentadentate

[a]*Center of Basic Molecular Science (CBMS), Department of Chemistry, Tsinghua University, Beijing 100084, China. E-mail: mtzhang@mail.tsinghua.edu.cn, zhanght18@tsinghua.org.cn*
[b]*Key Laboratory of Material Chemistry for Energy Conversion and Storage, Ministry of Education, Hubei Key Laboratory of Bioinorganic Chemistry and Materia Medica, Hubei Key Laboratory of Materials Chemistry and Service Failure, School of Chemistry and Chemical Engineering, Huazhong University of Science and Technology, Wuhan 430074, China. E-mail: jiayi@hust.edu.cn*

† Electronic supplementary information (ESI) available. See DOI: https://doi.org/10.1039/d4dt02872d

N5 ligands in Fe^{III}–OOH intermediates tend to favor homolytic cleavage of the O–O bond, leading to the generation of Fe^{IV}=O and $^{\bullet}$OH, which activates benzene for hydroxylation.[55]

Inspired by copper-containing metalloenzymes, such as tyrosinase and catechol oxidase,[56–61] which perform aromatic ring oxidation, copper-based catalysts have also attracted considerable attention due to their superior catalytic activity compared to other first-row transition metals, particularly in the cases of dicopper catalysts.[21–25,31,32] Notably, the Cu_2(6-hpa)(μ-OH) catalyst, with 6-hpa representing 1,2-bis[2-[bis(2-pyridylmethyl)aminomethyl]-6-pyridyl]ethane, exhibits a remarkable turnover number (TON) exceeding 12 000 for phenol production,[23] attributed to bimetallic cooperation catalysis *via* a μ–η^1:η^1-O_2 type dicopper peroxo intermediate. Research in Cu–oxygen chemistry has shown that ligand denticity can significantly influence the coordination geometries of key Cu–O_2 adducts and subsequently alter their reactivity, particularly regarding O–O bond cleavage.[61–66] In recent years, a diverse range of dicopper–oxygen adducts, including Cu(μ–η^1:η^1-O_2)Cu, Cu(μ–η^2:η^2-O_2)Cu, and Cu(μ-oxo)$_2$Cu intermediates, have been explored for the hydroxylation reaction of aromatic rings (Fig. 1a and b).[57,67–70] Meanwhile, the Cu(μ–η^1:η^2-O_2)Cu type peroxo intermediate remains largely uncharacterized in the context of selective benzene hydroxylation.

Recently, we developed a dicopper water oxidation catalyst $[Cu^{II}_2(TPMAN)(\mu\text{-}OH)(H_2O)]^{3+}$(**1**, Fig. 1c), featuring a nonsymmetric ligand TPMAN (= 1-(7-((bis(pyridin-2-ylmethyl)amino)methyl)-1,8-naphthyridin-2-yl)-*N*-methyl-*N*-(pyridin-2-ylmethyl)methanamine), in which two Cu^{II} ions respectively possess different free coordination sites. This structure leads to the formation of a μ–η^1:η^2-O_2 type dicopperperoxo intermediate, allowing for enhanced catalytic performance.[65] In this study, we employ this structurally well-defined dicopper complex for the direct hydroxylation of benzene with H_2O_2 as the oxidant, demonstrating exceptional catalytic activity (a TON of 14 000 within 29 hours) and selectivity (up to 97%) for phenol production. Mechanistic investigations reveal that the Cu(μ–η^1:η^2-O_2)Cu intermediate can be effectively reduced by H_2O_2, directly generating the Cu^{II}(μ-1,1-OOH)Cu^{I} intermediate, which facilitates O–O bond cleavage. The resulting Cu^{II}(μ-O$^{\bullet}$)Cu^{II}–OH species serves as the active entity for the electrophilic hydroxylation of benzene. Compared to previously reported dicopper catalysts,[23,57,67–70] our uniquely coordinated dicopper site alters the activation pathway of H_2O_2, yielding a distinct copper-oxyl intermediate that enhances the selectivity of benzene hydroxylation.

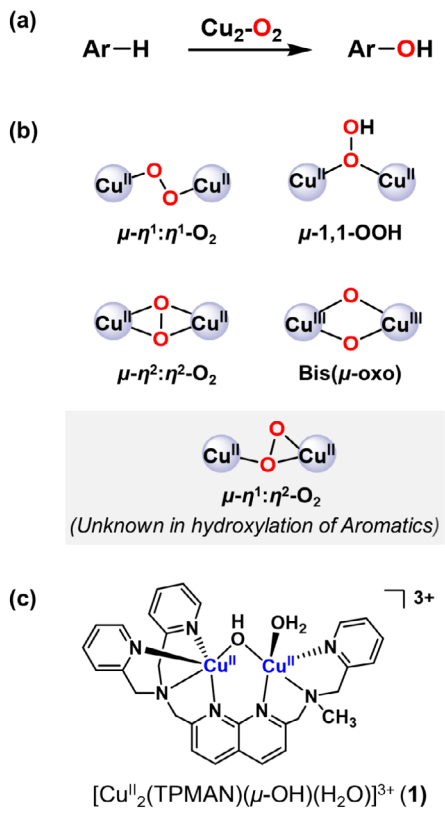

Fig. 1 (a) Hydroxylation of aromatics catalyzed by copper–oxygen intermediates; (b) different coordinated structures of dicopper–O_2 intermediates have been well studied; and (c) the molecular structure of the nonsymmetric dicopper catalyst $[Cu^{II}_2(TPMAN)(\mu\text{-}OH)(H_2O)]^{3+}$ (**1**) in this work.

Results and discussion

For the dicopper complex $[Cu^{II}_2(TPMAN)(\mu\text{-}OH)(H_2O)]^{3+}$ (**1**), the detailed synthetic procedure and characterization have been documented in our previous work.[65] Subsequently, we conducted the hydroxylation of benzene utilizing complex **1** as the catalyst and 30% hydrogen peroxide (H_2O_2) as the oxidant. Under representative reaction conditions, 30 mmol benzene was dissolved in 20 mL of acetonitrile (CH_3CN) and treated with 120 mmol H_2O_2 and 5 μmol triethylamine (Et_3N) as the base, with 1 μmol catalyst **1** under heating at 45 °C for 6 hours. Following the reaction, the mixture was extracted with chloroform ($CHCl_3$) and subsequently purified using a short neutral alumina column. After solvent removal, an analysis by ^{1}H NMR confirmed the formation of phenol in the residue. Building on this preliminary finding, we optimized the reaction conditions, focusing on the catalyst, the ratio of oxidant/benzene, base concentrations and reaction temperature (refer to Tables 1 and S1–S3, Fig. S1†), and the products were detected and quantified by gas chromatography (Fig. S2†). Notably, the method of oxidant addition, whether one-pot or sequential, did not significantly influence the reaction outcome. Examining varying amounts of Et_3N (Table S2†), we observed that when no Et_3N (entry 1) was added or when excess Et_3N was added (entry 3), the rate of phenol generation during the initial 7 hours was lower compared to when an optimal amount of Et_3N was employed (entry 2). However, after 24 hours, the final conversion ratios and yields were comparable across all trials. Intriguingly, extending the reaction time to approximately 44 hours in the presence of high con-

Table 1 The catalytic activity of the catalyst **1** at different temperatures

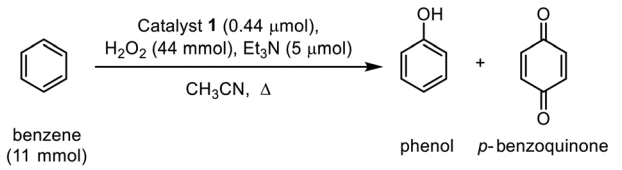

Entry	T (°C)	Conv.[a] (%)	Yield[b] (%)	Selectivity for phenol[c] (%)
1	45	25	3.4	78
2	65	61	6.7	92
3	70	52	7.3[d]	92
4	80	61	7.0[e]	92

Conditions: 11 mmol of benzene, 44 mmol of 30% H_2O_2, 0.44 μmol of catalyst **1**, and 5 μmol of Et_3N in 6.3 mL of CH_3CN. [a] Conversation% = n(consumed benzene)/n(starting benzene). [b] Yield% = n(phenol)/n-(starting benzene). [c] Selectivity is calculated based on the products detected by GC. Selectivity% = n(phenol)/(n(phenol) + n-(benzoquinone)). The reaction time is 20 h. [d] 24 h. [e] 12 h.

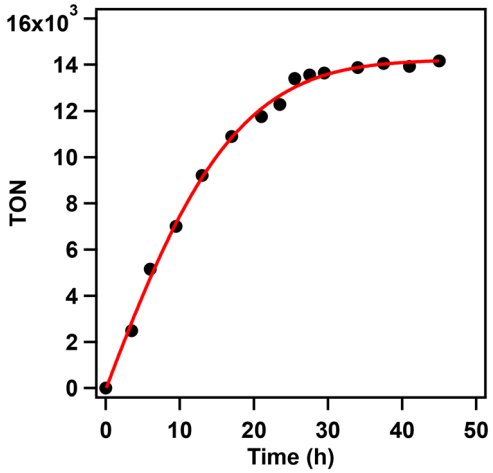

Fig. 2 Time profile formation of phenol in the hydroxylation of benzene using catalyst **1** (0.05 μmol) with 11 mmol of benzene, 44 mmol of 30% H_2O_2, and 5 μmol of Et_3N in 6.3 mL of CH_3CN at 65 °C.

centrations of Et_3N resulted in catalytic selectivity reaching 100% (entry 3). We also evaluated various alternative bases (Table S3†), which exhibited performance analogous to that of Et_3N. Additionally, the molar ratio of H_2O_2 to benzene significantly impacted the oxidation results (Table S1, entries 2, 4, and 5†). At a lower H_2O_2-to-benzene ratio, the reaction selectivity for phenol increased; however, this selectivity decreased to about 70% as the ratio increased. Conversely, the yield of phenol improved with higher ratios of hydrogen peroxide. Finally, we further optimized the catalytic activity of catalyst **1** by varying the reaction temperatures (Table 1). Our results indicate that moderate temperature enhances catalytic performance. At 65 °C after 20 h, the yield of phenol reached approximately 6.7%, based on the initial amount of benzene, with the selectivity reaching up to 92%. Notably, increasing the temperature beyond 70 °C did not yield any significant improvement in the reaction outcome.

Subsequent investigations focused on the long-term catalytic performance of benzene hydroxylation using catalyst **1**, with the time courses of phenol production illustrated in Fig. 2 and S5.† At a temperature of 65 °C, catalyst **1** exhibits a maximum turnover frequency (TOF_{max}) of approximately 859 h^{-1} and a maximum turnover number (TON) of 14 000 after 29 hours, resulting in a phenol yield of 6.1% and a remarkable selectivity of 97%. This impressive catalytic performance is comparable to the highest TON for benzene hydroxylation using H_2O_2 in homogeneous catalysis (Table S4†).[23] At a reduced reaction temperature of 45 °C, catalyst **1** still displayed a noteworthy TON of 8500 for phenol (Fig. S5†). It is important to note that *p*-benzoquinone was also generated during the early stages of the reaction alongside phenol, indicating that *p*-benzoquinone is a product of phenol over-oxidation.[33] However, the yield of *p*-benzoquinone remained consistently low throughout the reaction period (Fig. S3 and S4†). These findings suggest that this nonsymmetric dicopper catalyst is capable of selectively promoting the hydroxylation of benzene to phenol, achieving the highest TON reported to date.

To further explore the reactivity of the active species, we examined various aromatic substrates, including phenol, toluene, and nitrobenzene, under identical reaction conditions (Table 2 and Fig. S6–S8†). For phenol, *p*-benzoquinone was the only product detected initially, while catechol was observed after 12 h, resulting in a total TON of 3200 after 23 hours. Using toluene as the substrate yielded *o*-cresol, *p*-cresol, and benzaldehyde as the major products, with a total TON of 1700 after 23 hours. The ratio of aromatic to aliphatic oxidations

Table 2 Product analysis of oxidation of different substrates using catalyst **1**

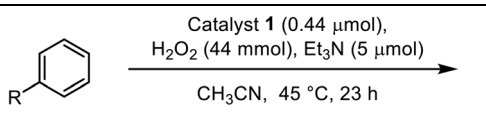

R = H, OH, CH_3, NO_2

Entry[a]	Substrate	Products [%] (*o*/*p*/*m*)	TOF[c] (h^{-1})	TON[d]
1	Benzene	Phenol [83] *p*-Benzoquinone [17]	196	1200
2[b]	Benzene	Phenol [97] *p*-Benzoquinone [3]	859	14 000
3	Phenol	Catechol [40] *p*-Benzoquinone [60]	332	3200
4	Toluene	Cresol [73] (60 : 40 : trace) Benzaldehyde [27]	245	1700
5	Nitrobenzene	No product	—	—

[a] 0.44 μmol catalyst, 5 μmol base (Et_3N), 44 mmol H_2O_2 (30%), 6.3 mL CH_3CN, 45 °C, and 23 h. The substrate: **1** and **2**: 11 mmol benzene; **3**: 8.5 mmol phenol; **4**: 8.2 mmol toluene; and **5**: 8.2 mmol nitrobenzene. [b] 0.05 μmol catalyst, 5 μmol base (Et_3N), 44 mmol H_2O_2 (30%), 6.3 mL CH_3CN, 65 °C, and 23 h. [c] TOF of all products after 23 h. [d] TON of all products after 23 h.

was approximately 2.7 : 1.0, and the distribution of cresols was about 1.6 : 1.0 : 0 (*o* : *p* : *m*), which is in contrast with the ratios typically associated with the Fenton mechanism.[71] In the case of nitrobenzene, neither *o*-nitrophenol nor *p*-nitrophenol was detected. Consequently, the relative reactivity order based on the TON under the same reaction conditions was determined as follows: phenol > toluene > benzene ≫ nitrobenzene. This trend highlights the propensity for oxidation to occur preferentially on aromatic rings with electron-donating substituents, and the observed sensitivity to the electronic density of the aromatic ring suggests that the oxidation mechanism is likely metal-mediated through an electrophilic intermediate rather than involving radical pathways.

To investigate the reaction mechanism in depth, 5,5′-dimethyl-1-pyrroline *N*-oxide (DMPO) was employed as a radical scavenger to assess the formation of hydroxyl (˙OH) or hydroperoxyl (˙OOH) radicals, which are potential active species in the Fenton mechanism. As demonstrated in Fig. 3a, the rates of phenol production in the presence of either 0.5 mM or 5.0 mM DMPO were consistent with the rate observed in the absence of DMPO. Additionally, the introduction of carbon tetrachloride (CCl_4) did not yield detectable chlorobenzene or biphenyl species at any point during the reaction. These results indicate that no obvious radical species, including hydroxyl (˙OH) or hydroperoxyl (˙OOH) radicals, exist in the reaction solution to catalyze hydroxylation of benzene through the radical-chain mechanism. Furthermore, the kinetic isotope effect (KIE) was investigated using hexadeuterio-benzene (d_6-benzene) as a substrate, resulting in a KIE value of 1.05 determined from the initial rates of phenol production (Fig. 3b). This value suggests that the C–H bond cleavage of benzene is not part of the rate-determining step. This relatively low KIE value differs significantly from the KIE (approximately 1.7–1.8) reported for Fenton-type hydroxylation[72] or those existing values greater than 4 for rebound mechanisms.[42,73,74] Additionally, a standard selectivity test for the reaction involving the ˙OH radical was conducted using methylcyclohexane under standard conditions.[75] The gas chromatography (GC) results reveal that the product ratio of tertiary alcohol to secondary alcohol is approximately 1 : 15 (Fig. S9†), which does not align with the expected selectivity ratio of 3 : 10 (ref. 75) for the ˙OH radical mechanism. Furthermore, the lack of hydroxylation reactivity observed with nitrobenzene is inconsistent with the Fenton-type mechanism.[72] These findings seem to contradict the Fenton-type mechanism and the rebound process, while they are consistent with an electrophilic aromatic substitution mechanism.[51,68,76]

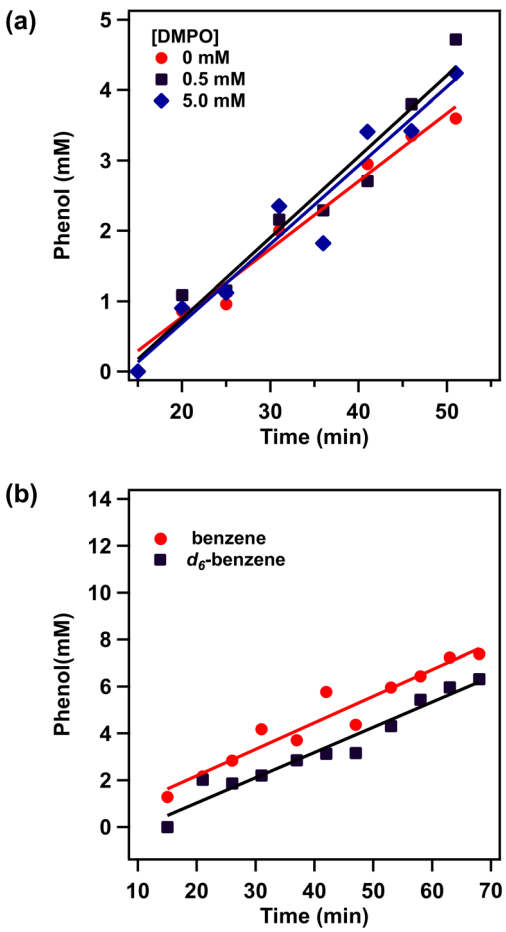

Fig. 3 (a) Time courses for phenol production in the reaction of benzene oxidation catalyzed by **1** in the absence (red) and presence of DMPO [0.5 mM (black) and 5 mM (blue)] during the first hour. (b) Time courses for phenol production in the oxidation of benzene (red) and d_6-benzene (black) as the substrates catalyzed by **1** under the conditions described.

Moreover, the reaction kinetics of benzene oxidation catalyzed by **1** was analyzed through the initial rates of phenol production. As depicted in Fig. S10–S12,† the concentrations of benzene, catalyst, and H_2O_2 each exhibit a first-order linear relationship with the rate of phenol production. Based on these dependencies, the kinetic equation governing the benzene oxidation reaction can be articulated as:

$$d[\text{Phenol}]/\text{d}t = k_{\text{cat}}[\text{catalyst } \mathbf{1}][\text{benzene}][H_2O_2],$$

where k_{cat} represents the catalytic rate constant.

Based on the experimental results outlined above, computational studies were performed to elucidate the details of the catalytic mechanism. The initial [Cu^{II}_2(TPMAN)(μ-OH)(H_2O)] species (labeled as complex **1**, Fig. 4a, for detailed structure, see Table S5†), featuring two penta-coordinated copper sites, can react with H_2O_2 to form the Cu^{II}(μ–η^1:η^1-OOH)Cu^{II} intermediate **Int1** (Table S5†), accompanied by an energy release of 3.8 kcal mol^{-1}. Following this, the deprotonation of **Int1** by Et_3N occurs, and the generated dicopperperoxo **Int2** ([Cu^{II}(μ–η^1:η^2-O_2)Cu^{II}], Table S6) is then reduced by 1/2 equivalent of H_2O_2, leading to the formation of **Int3** ([Cu^{II}(μ-1,1-OOH)Cu^{I}], Table S6†), which has been confirmed to be a vital intermediate in our previous study,[64,77] and 1/2 equivalent of O_2. The deprotonation process is calculated to be exergonic by 10.0 kcal mol^{-1}, while the reduction of **Int2** to **Int3** is endergonic by +1.8 kcal mol^{-1}; thus, **Int2** has been assigned as the starting point of the energy profile (Fig. 4b). Additionally, the possibility of a direct electrophilic attack of benzene on the

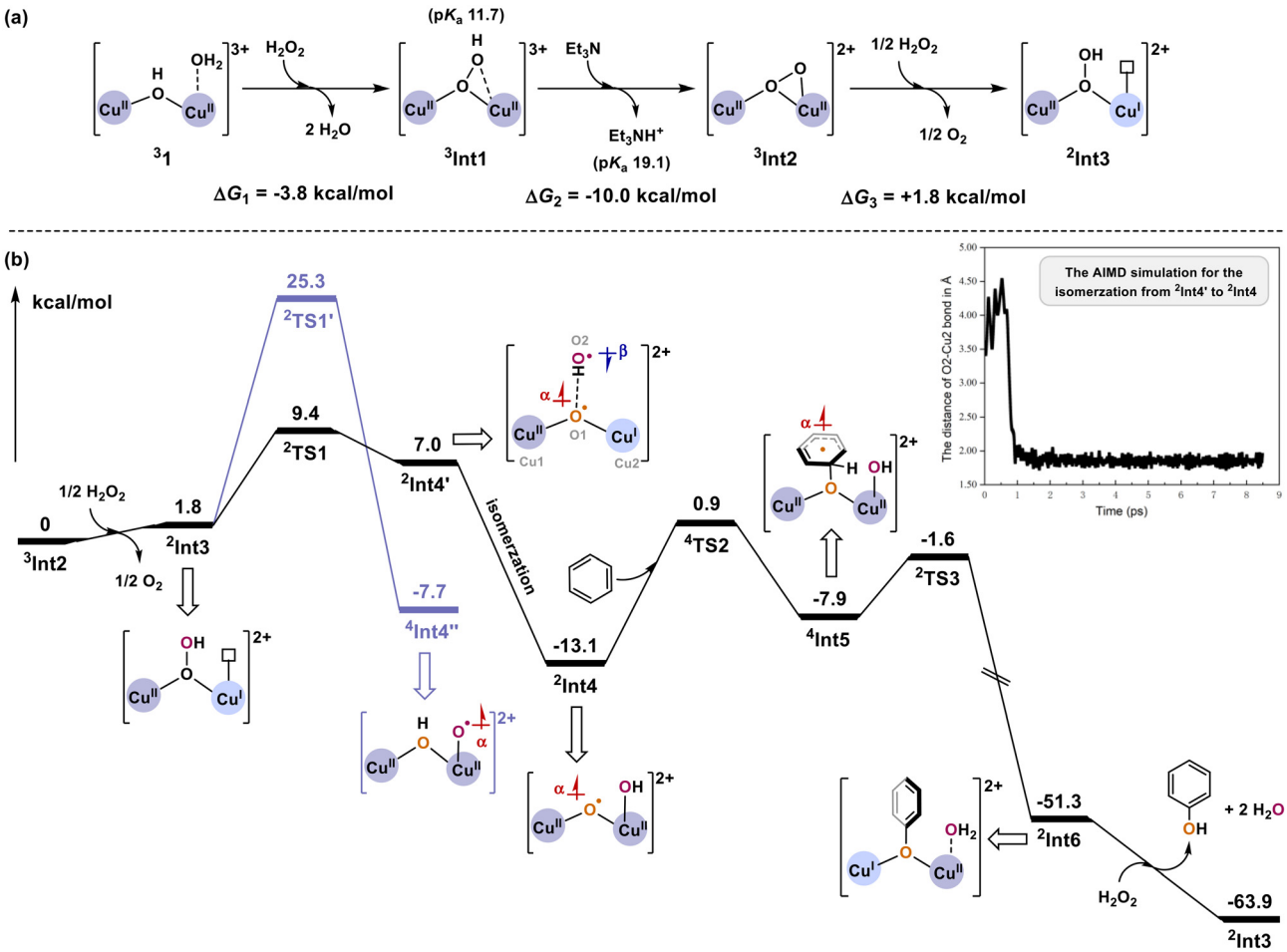

Fig. 4 (a) The generated process of **Int3** begins with the nonsymmetric dicopper catalyst $[Cu^{II}_2(TPMAN)(\mu\text{-}OH)(H_2O)]^{3+}$(complex **1**); the left superscript of the name of stationary points indicates the spin multiplicity. (b) Gibbs energy diagram for the formation of phenol catalyzed by **Int3**. The core structures of important intermediates are displayed, and the half arrow near the structure represents the spin direction of the unpaired electron. The AIMD simulation for the isomerization process is also shown.

peroxide moiety of **Int2** can be ruled out, as the calculated energy barrier is +40.7 kcal mol^{-1} (Fig. S13, and Table S7†).

Subsequently, **Int3** undergoes a homolytic O–OH bond cleavage process *via* **TS1**, generating the diradical intermediate **Int4′** (Table S8†) with a barrier of +7.6 kcal mol^{-1}. The optimized structure of the transition state **TS1** is depicted in Fig. 5. **TS1** is a doublet and the Mulliken spin populations on Cu1, O1, Cu2, and O2 are 0.62, 0.42, 0.53, and −0.89, respectively. Frequency analysis of ^{2}**TS1** gives only one imaginary frequency of 295.5*i* cm^{-1}, related to the cleavage of the O1–O2 bond. The length of the breaking O1–O2 bond and the forming hydrogen bond of O1–H1 measures 2.38 Å and 1.91 Å, respectively. The *Ab Initio* Molecular Dynamics (AIMD) calculations for **Int4′** indicate that **Int4′** can be regarded as a metastable intermediate since it can rapidly (within one ps, Fig. S14 and S15†) isomerize to the $Cu^{II}(\mu\text{-}O^{\bullet})Cu^{II}$–OH intermediate **Int4** without any applied potential. **Int4** lies at −14.9 kcal mol^{-1} relative to **Int3**, with a ground state of the doublet. In ^{2}**Int4** (Fig. 5), the distance of the formed Cu2–O2 bond is 1.80 Å, consisting of a β-electron donated by the O2 moiety and an α-electron from Cu2. It should be pointed out that the decrease in Mulliken spin population on O1 (a Mulliken spin population of 0.30) and Cu2 (a Mulliken spin population of −0.11) atoms is due to the interaction of the remaining β-electron on Cu2 with the O1 radical, which possesses an α-electron. Additionally, the formation of the $Cu^{II}(\mu\text{-}OH)Cu^{II}$–$O^{\bullet}$ intermediate **Int4″** (Table S9) has also been considered, with a barrier of +23.5 kcal mol^{-1} (**TS1′**, Fig. 4b, Table S9†) relative to **Int3** and +15.9 kcal mol^{-1} higher than that of **TS1**. Compared to **Int4″**, the formation of **Int4** is kinetically more favorable; therefore, the pathway initiating from **Int4** is described in detail here, and other pathways will be briefly discussed when necessary.

The O1 radical in **Int4** then electrophilically attacks the benzene substrate directly, forming the essential O1–C1 bond through a quartet transition state **TS2**, with a significant Mulliken spin population distributed at the O1 (a Mulliken spin population of 0.69) and benzene (a Mulliken spin population of 0.53). The barrier of **TS2** is calculated to be +14.0 kcal mol^{-1} relative to **Int4** plus benzene, and the length of the O1–

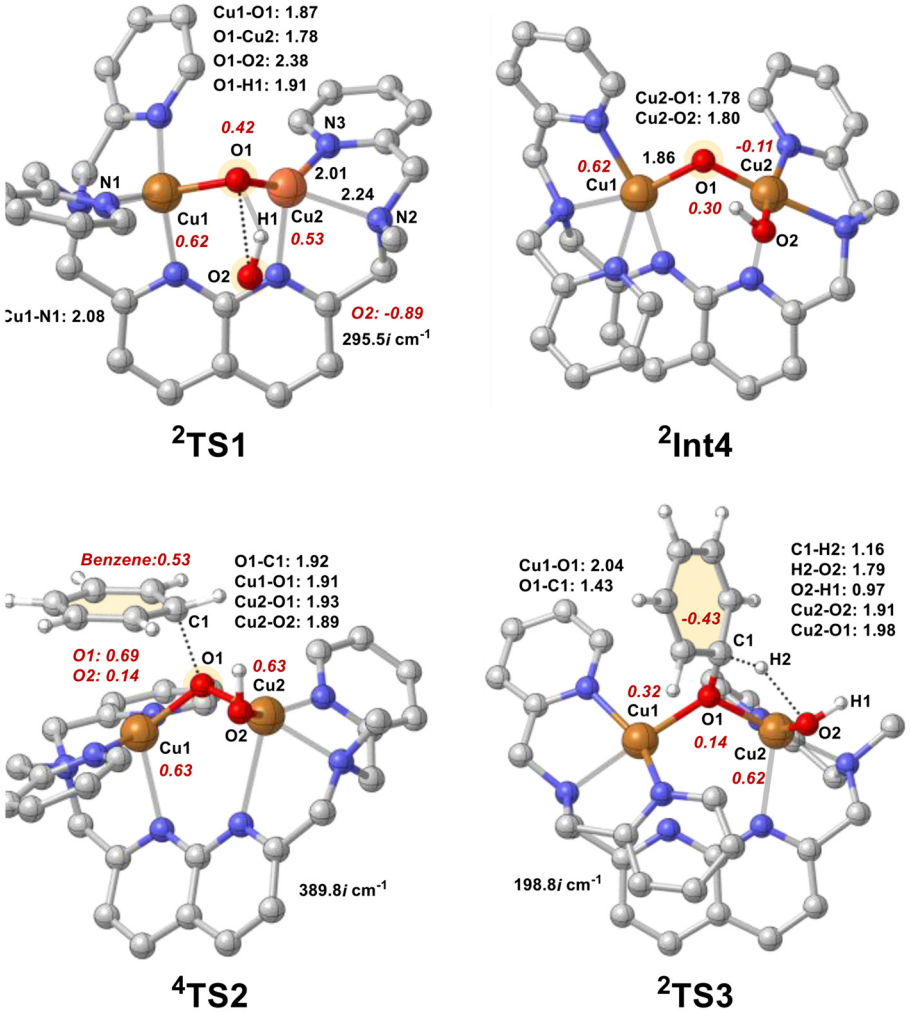

Fig. 5 Optimized structures of **TS1**, **Int4**, **TS2**, and **TS3**. Distances are shown in Å in black, Mulliken spin populations on selected atoms are shown in red, and the imaginary frequencies (in cm^{-1}) for transition states are also shown. For clarity, unimportant hydrogen atoms are not shown.

C1 bond in **TS2** is 1.92 Å. The generated ^{4}**Int5** (Table S10†) is +5.2 kcal mol^{-1} higher in energy than ^{2}**Int4**, which contains a benzene radical (a Mulliken spin population of 0.92) and two Cu^{II} ion centers. Notably, when nitrobenzene acts as a substrate, the O1–C1 bond formation *via* the electrophilic attack of **Int4** needs to overcome higher barriers of about +15.4–16.7 kcal mol^{-1} (Tables S11 and S12†), consistent with the above-mentioned experimental findings. If CH_3CN as the substrate is activated by **Int4** abstracting the hydrogen atom, the energy barrier is also obviously higher than that of the benzene activation (Tables S11 and S12†). Thus, the CH_3CN solvent would not interfere with the benzene hydroxylation reaction, and no CH_3CN-related products are observed in the gas chromatograph (Fig. S8†). These results further confirm that **Int4** activates the benzene *via* electrophilic attack rather than the abstraction of hydrogen atoms.

The ground state of transition state **TS3** (Fig. 5) is a doublet, showing that the electron on the benzene radical is flipped (a Mulliken spin population of −0.43) and coupled with $Cu1^{II}$ (a Mulliken spin population of 0.32) antiferromagnetically. **TS3** involves proton transfer from C1 to the OH moiety and electron transfer from the benzene radical to the $Cu1^{II}$ ion. The C1–H2, H2–O2, and Cu2–O1 bond distances in ^{2}**TS3** are 1.16, 1.79, and 1.98 Å, respectively; the barrier of **TS3** is +6.3 kcal mol^{-1}, and the imaginary frequency is 198.8*i* cm^{-1}. Downhill from **TS3**, **Int6** (Table S10†) is formed, and it is associated with a large energy release of 49.7 kcal mol^{-1} relative to **Int5**. Based on the Mulliken spin population analysis of **Int6**, Cu1 accepts the β-electron transferred from the benzene radical, resulting in its oxidation state becoming +1; Cu2 remains at +2 and coordinated with the generated H_2O. Finally, the oxidant H_2O_2 reacts with **Int6**, yielding H_2O molecules and the target product phenol and regenerating species **Int3** to catalyze the next cycle.

According to the Gibbs free energy diagram derived from the DFT calculations, the electrophilic attack of the catalytically active species **Int4** on the benzene (**TS2**) is the rate-determining step, with a calculated barrier of +14.0 kcal mol^{-1}. This finding aligns with the experimental evidence indicating that the C–H bond cleavage of benzene was not involved in the

rate-determining step. The additive base (Et_3N) is solely responsible for the deprotonation of **Int1** to form **Int2**, initiating the catalytic process *via* the generated active intermediate **Int3**. Moreover, the generation of catalytically active species **Int4** ($Cu^{II}(\mu\text{-}O^{\bullet})Cu^{II}$–OH) benefits from the nonsymmetric coordination geometry of **Int3**, which provides vacant coordination sites to receive the OH group.

Conclusions

In this study, we successfully demonstrated the efficacy of a nonsymmetric dicopper water oxidation catalyst ($[Cu^{II}_2(TPMAN)(\mu\text{-}OH)(H_2O)]^{3+}$, **1**) for the direct oxidation of benzene to phenol using the environmentally benign oxidant H_2O_2. Its catalytic performance was found to be comparable to the most effective copper-based molecular catalyst reported to date. Investigations into the substituent effects on the benzene ring revealed that electron-donating groups enhanced the oxidation reaction, while electron-withdrawing groups exhibited the opposite effect, thereby suggesting the involvement of an electrophilically active intermediate in the reaction mechanism. Notably, experimental results indicating no interaction with the radical scavenger DMPO, coupled with a kinetic isotope effect (KIE) of 1.05 and an inconsistent standard selectivity test of the $^{\bullet}OH$ radical, contradict the traditional Fenton and rebound mechanisms as pathways for this reaction. Additionally, density functional theory (DFT) calculations elucidated how the unique geometrical arrangement of the dicopper core modulates the activation pathway of H_2O_2, leading to the formation of an electrophilic $Cu^{II}(\mu\text{-}O^{\bullet})Cu^{II}$–OH species. This species is pivotal in facilitating the selective hydroxylation of benzene to phenol in a controllable manner. Overall, this work advances the understanding of the mechanism underlying the one-step oxidation of benzene and provides valuable insights for the design of efficient catalysts for benzene hydroxylation.

Experimental section

Materials and instruments

Chemicals were obtained commercially with the highest purity and were used without further purification unless otherwise specified. The ligand TPMAN was synthesized following our previous procedure.[65] Gas chromatography (GC) data were collected using a Shimadzu 2010 Plus GC system with an Rxi®-5 ms capillary column with nitrobenzene utilized as a standard. NMR spectra were recorded on a 400 MHz Bruker BioSpin Advance III NMR spectrometer.

Synthesis of $[Cu^{II}_2(TPMAN)(\mu\text{-}OH)(H_2O)](CF_3SO_3)_3$ ($\mathbf{1(OTf)_3}$)

The synthesis procedure of **1** has been reported in our previous work.[65] A solution of the TPMAN ligand (90 mg, 0.19 mmol) in acetonitrile (10 mL), was added dropwise into a stirred solution of $Cu(CF_3SO_3)_2$ (138.80 mg, 0.38 mmol) in 8 mL of MeCN : H_2O (v : v = 3 : 1). The solution was rapidly converted to deep blue-green and allowed to stir overnight. The resulting solution was concentrated under reduced pressure and an oil was obtained. Ether (20 mL) was added, and a blue crude product was isolated after ultrasonic washing of the resulting mixture for several minutes, followed by copious washing with ethyl ether. The syrup product was recrystallized from acetonitrile and ether. The product was obtained as a blue powder (80 mg, yield 35%). HRMS (ESI^+): m/z $[M - H_2O\text{-}3(CF_3SO_3)]^{3+}$, exp.: 206.0361, cal.: 206.0368; $[M - H_2O\text{-}2(CF_3SO_3)]^{2+}$, exp.: 383.5371, cal.: 383.5312. Elemental analysis for $C_{32}H_{32}Cu_2F_9N_7O_{11}S_3$, calcd: C, 35.43; H, 2.97; N, 9.04; found: C, 35.19; H, 3.57; N, 8.76.

Catalytic reaction conditions for the hydroxylation of aromatic compounds

Under an argon atmosphere, a solution containing compound **1** (0.48 mg, 0.44 μmol), substrates (benzene (860 mg, 11 mmol), toluene (780 mg, 8.5 mmol), phenol (770 mg, 8.2 mmol), and nitrobenzene (1010 mg, 8.2 mmol)), and triethylamine (Et_3N) (0.5 mg, 5.0 μmol) was prepared in acetonitrile (6.3 mL) within a Schlenk flask and heated to 65 °C while stirring. Subsequently, 4.5 mL of 30% aqueous hydrogen peroxide (H_2O_2, 44 mmol) was introduced under an argon atmosphere. A portion of the reaction solution was extracted using a syringe, dried with anhydrous sodium sulfate (Na_2SO_4), and then analyzed by gas chromatography (GC), using nitrobenzene as a standard.

Calibration solution preparation

Calibration solutions were prepared to ascertain the correction factors (f_i). The calibration curves were established by plotting the linear relationship between the peak area ratio (S_i/S_0) and the mass ratio (m_i/m_0). Here, S_i and S_0 denote the peak areas of the analyte and the internal standard, respectively, while m_i and m_0 refer to the masses of the analyte and the internal standard.

$$\frac{m_i}{m_0} = f_i \times \frac{S_i}{S_0}. \quad (1)$$

Quantification of the hydroxylation products

Correction factors were used to quantify the mass of the hydroxylation products (m_s) using eqn (2). S_s and S_0 are the peak areas of the analyte and internal standard, while m_s and m_0 are the masses of the analyte and internal standard, respectively.

$$m_s = f_i \times \frac{S_s}{S_0} \times m_0. \quad (2)$$

Data availability

The data supporting this article have been included as part of the ESI.†

Conflicts of interest

There are no conflicts to declare.

Acknowledgements

This work was supported by the National Natural Science Foundation of China (NSFC Grant No. 219330007 and 22193011).

References

1 R. A. Sheldon and J. K. Kochi, in *Metal-Catalyzed Oxidations of Organic Compounds*, ed. R. A. Sheldon and J. K. Kochi, AcademicPress, New York, 1981, pp. 315–339.
2 M. Weber and M. Kleine-Boymann, in *Ullmann's Encyclopedia of Industrial Chemistry*, Wiley-VCH, Weinheim, Germany, 2000.
3 K. Weissermel and H. J. Arpe, *Industrial Organic Chemistry*, John Wiley & Sons, 3rd edn, 2008.
4 R. Molinari and T. Poerio, *Asia-Pac. J. Chem. Eng.*, 2009, **5**, 191–206.
5 R. J. Schmidt, *Appl. Catal., A*, 2005, **280**, 89–103.
6 D. P. Ivanov, L. V. Pirutko and G. I. Panov, *J. Catal.*, 2014, **311**, 424–432.
7 R. Bal, M. Tada, T. Sasaki and Y. Iwasawa, *Angew. Chem., Int. Ed.*, 2006, **45**, 448–452.
8 J. W. Han, J. Jung, Y. M. Lee, W. Nam and S. Fukuzumi, *Chem. Sci.*, 2017, **8**, 7119–7125.
9 S. S. Acharyya, S. Ghosh, R. Tiwari, C. Pendem, T. Sasaki and R. Bal, *ACS Catal.*, 2015, **5**, 2850–2858.
10 Y. Zhu, W. Sun, J. Luo, W. Chen, T. Cao, L. Zheng, J. Dong, J. Zhang, M. Zhang, Y. Han, C. Chen, Q. Peng, D. Wang and Y. Li, *Nat. Commun.*, 2018, **9**, 3861.
11 S. Bhandari, R. Khatun, T. S. Khan, D. Khurana, M. K. Poddar, A. Shukla, V. V. D. N. Prasad and R. Bal, *Green Chem.*, 2022, **24**, 9303.
12 J. Xie, X. Li, J. Guo, L. Luo, J. J. Delgado, N. Martsinovich and J. Tang, *Nat. Commun.*, 2023, **14**, 4431.
13 Y.-J. Lyu, T. Qi, H.-Q. Yang and C.-W. Hu, *Catal. Sci. Technol.*, 2018, **8**, 176–186.
14 G. Wen, S. Wu, B. Li, C. Dai and D. S. Su, *Angew. Chem., Int. Ed.*, 2015, **54**, 4105–4109.
15 S. Verma, R. B. N. Baig, M. N. Nadagouda and R. S. Varma, *ACS Sustainable Chem. Eng.*, 2017, **5**, 3637–3640.
16 L. Meng, X. Zhu and E. J. M. Hensen, *ACS Catal.*, 2017, **7**, 2709–2719.
17 W. Laufer, J. P. M. Niederer and W. F. Hoelderich, *Adv. Synth. Catal.*, 2002, **344**, 1084–1089.
18 Y. Zhao, H. Cao, L. Tao, Z. Qiao and C. Ding, *Dalton Trans.*, 2023, **52**, 5399–5417.
19 T. Shen, Z. Song, J. Li, S. Bai, G. Liu, X. Sun, S. Li, W. Chen, L. Zheng and Y. F. Song, *Small*, 2023, **19**, e2303420.
20 G. Capocasa, G. Olivo, A. Barbieri, O. Lanzalunga and S. Di Stefano, *Catal. Sci. Technol.*, 2017, **7**, 5677–5686.
21 L. Vilella, A. Conde, D. Balcells, M. M. Díaz-Requejo, A. Lledós and P. J. Pérez, *Chem. Sci.*, 2017, **8**, 8373–8383.
22 A. Conde, M. Mar Díaz-Requejo and P. J. Pérez, *Chem. Commun.*, 2011, **47**, 8154–8156.
23 T. Tsuji, A. A. Zaoputra, Y. Hitomi, K. Mieda, T. Ogura, Y. Shiota, K. Yoshizawa, H. Sato and M. Kodera, *Angew. Chem., Int. Ed.*, 2017, **56**, 7779–7782.
24 M. Yamada, K. D. Karlin and S. Fukuzumi, *Chem. Sci.*, 2016, **7**, 2856–2863.
25 L. Wu, W. Zhong, B. Xu, Z. Wei and X. Liu, *Dalton Trans.*, 2015, **44**, 8013–8020.
26 O. Shoji, S. Yanagisawa, J. K. Stanfield, K. Suzuki, Z. Cong, H. Sugimoto, Y. Shiro and Y. Watanabe, *Angew. Chem., Int. Ed.*, 2017, **56**, 10324–10329.
27 K. Ikeda, K. Yoshizawa and Y. Shiota, *Inorg. Chem.*, 2021, **61**, 10–14.
28 H. Qi, D. Xu, J. Lin and W. Sun, *Mol. Catal.*, 2022, **528**, 112441.
29 Y. Morimoto, S. Bunno, N. Fujieda, H. Sugimoto and S. Itoh, *J. Am. Chem. Soc.*, 2015, **137**, 5867–5870.
30 S. Muthuramalingam, K. Anandababu, M. Velusamy and R. Mayilmurugan, *Catal. Sci. Technol.*, 2019, **9**, 5991–6001.
31 E. Borrego, L. Tiessler-Sala, J. J. Lázaro, A. Caballero, P. J. Pérez and A. Lledós, *Organometallics*, 2022, **41**, 1892–1904.
32 S. Kumari, S. Muthuramalingam, A. K. Dhara, U. P. Singh, R. Mayilmurugan and K. Ghosh, *Dalton Trans.*, 2020, **49**, 13829–13839.
33 J. Kumari, S. M. Mobin, S. Mukhopadhyay and K. M. Vyas, *Inorg. Chem. Commun.*, 2019, **105**, 217–220.
34 L. Carneiro and A. R. Silva, *Catal. Sci. Technol.*, 2016, **6**, 8166–8176.
35 O. Y. Lyakin, A. M. Zima, N. V. Tkachenko, K. P. Bryliakov and E. P. Talsi, *ACS Catal.*, 2018, **8**, 5255–5260.
36 N. V. Tkachenko, R. V. Ottenbacher, O. Y. Lyakin, A. M. Zima, D. G. Samsonenko, E. P. Talsi and K. P. Bryliakov, *ChemCatChem*, 2018, **10**, 4052–4057.
37 N. V. Tkachenko, O. Y. Lyakin, A. M. Zima, E. P. Talsi and K. P. Bryliakov, *J. Organomet. Chem.*, 2018, **871**, 130–134.
38 A. M. Zima, O. Y. Lyakin, D. P. Lubov, K. P. Bryliakov and E. P. Talsi, *Mol. Catal.*, 2020, **483**, 110708.
39 E. Masferrer-Rius, M. Borrell, M. Lutz, M. Costas and R. J. M. K. Gebbink, *Adv. Synth. Catal.*, 2021, **363**, 3783–3795.
40 S. R. Kalahrudi, A. Shakeri, A. Ghadimi and H. Mahdavi, *J. Membr. Sci.*, 2020, **611**, 118230.
41 C. Walling and R. A. Johnson, *J. Am. Chem. Soc.*, 1975, **97**, 363–367.
42 A. E. Shilov and G. B. Shul'pin, *Chem. Rev.*, 1997, **97**, 2879–2932.
43 S. Ito, A. Mitarai, K. Hikino, M. Hirama and K. Sasaki, *J. Org. Chem.*, 1992, **57**, 6937–6941.
44 X. Jia, C. Liu, X. Xu, F. Wang, W. Li, L. Zhang, S. Jiao, G. Zhu and X. Wang, *RSC Adv.*, 2023, **13**, 19140–19148.
45 L. T. Burka, T. M. Plucinski and T. L. Macdonald, *Proc. Natl. Acad. Sci. U. S. A.*, 1983, **80**, 6680–6684.

46 S. P. de Visser and S. Shaik, *J. Am. Chem. Soc.*, 2003, **125**, 7413–7424.
47 C. M. Bathelt, L. Ridder, A. J. Mulholland and J. N. Harvey, *J. Am. Chem. Soc.*, 2003, **125**, 15004–15005.
48 M.-J. Kang, W. J. Song, A.-R. Han, Y. S. Choi, H. G. Jang and W. Nam, *J. Org. Chem.*, 2007, **72**, 6301–6304.
49 M. Asaka and H. Fujii, *J. Am. Chem. Soc.*, 2016, **138**, 8048–8051.
50 S. Shaik, P. Milko, P. Schyman, D. Usharani and H. Chen, *J. Chem. Theory Comput.*, 2011, **7**, 327–339.
51 S. Muthuramalingam, K. Anandababu, M. Velusamy and R. Mayilmurugan, *Inorg. Chem.*, 2020, **59**, 5918–5928.
52 A. Rajeev, M. Balamurugan and M. Sankaralingam, *ACS Catal.*, 2022, **12**, 9953–9982.
53 B. Xu, W. Zhong, Z. Wei, H. Wang, J. Liu, L. Wu, Y. Feng and X. Liu, *Dalton Trans.*, 2014, **43**, 15337–15345.
54 J. N. Rebilly, W. Zhang, C. Herrero, H. Dridi, K. Senechal-David, R. Guillot and F. Banse, *Chem. – Eur. J.*, 2020, **26**, 659–668.
55 S. Xu, A. Draksharapu, W. Rasheed and L. Que, Jr., *J. Am. Chem. Soc.*, 2019, **141**, 16093–16107.
56 L. M. Mirica, M. Vance, D. J. Rudd, B. Hedman, K. O. Hodgson, E. I. Solomon and T. D. P. Stack, *Science*, 2005, **308**, 1890–1892.
57 E. A. Lewis and W. B. Tolman, *Chem. Rev.*, 2004, **104**, 1047–1076.
58 L. Chiang, W. Keown, C. Citek, E. C. Wasinger and T. D. Stack, *Angew. Chem., Int. Ed.*, 2016, **55**, 10453–10457.
59 A. Hoffmann, C. Citek, S. Binder, A. Goos, M. Rubhausen, O. Troeppner, I. Ivanovic-Burmazovic, E. C. Wasinger, T. D. Stack and S. Herres-Pawlis, *Angew. Chem., Int. Ed.*, 2013, **52**, 5398–5401.
60 M. F. Qayyum, R. Sarangi, K. Fujisawa, T. D. P. Stack, K. D. Karlin, K. O. Hodgson, B. Hedman and E. I. Solomon, *J. Am. Chem. Soc.*, 2013, **135**, 17417–17431.
61 C. E. Elwell, N. L. Gagnon, B. D. Neisen, D. Dhar, A. D. Spaeth, G. M. Yee and W. B. Tolman, *Chem. Rev.*, 2017, **117**, 2059–2107.
62 S. M. Adam, G. B. Wijeratne, P. J. Rogler, D. E. Diaz, D. A. Quist, J. J. Liu and K. D. Karlin, *Chem. Rev.*, 2018, **118**, 10840–11022.
63 H.-T. Zhang, F. Xie, Y.-H. Guo, Y. Xiao and M.-T. Zhang, *Angew. Chem., Int. Ed.*, 2023, **62**, e202310775.
64 X.-J. Su, M. Gao, L. Jiao, R.-Z. Liao, P. E. M. Siegbahn, J.-P. Cheng and M.-T. Zhang, *Angew. Chem., Int. Ed.*, 2015, **54**, 4909–4914.
65 Q.-Q. Hu, X.-J. Su and M.-T. Zhang, *Inorg. Chem.*, 2018, **57**, 10481–10484.
66 X.-J. Su, C. Zheng, Q.-Q. Hu, H.-Y. Du, R.-Z. Liao and M.-T. Zhang, *Dalton Trans.*, 2018, **47**, 8670–8675.
67 A. Kunishita, J. D. Scanlon, H. Ishimaru, K. Honda, T. Ogura, M. Suzuki, C. J. Cramer and S. Itoh, *Inorg. Chem.*, 2008, **47**, 8222–8232.
68 P. L. Holland, K. R. Rodgers and W. B. Tolman, *Angew. Chem., Int. Ed.*, 1999, **38**, 1139–1142.
69 G. Battaini, E. Monzani, A. Perotti, C. Para, L. Casella, L. Santagostini, M. Gullotti, R. Dillinger, C. Näther and F. Tuczek, *J. Am. Chem. Soc.*, 2003, **125**, 4185–4198.
70 T. Abe, Y. Kametani, K. Yoshizawa and Y. Shiota, *Inorg. Chem.*, 2021, **60**, 4599–4609.
71 H. Marusawa, K. Ichikawa, N. Narita, H. Murakami, K. Ito and T. Tezuka, *Bioorg. Med. Chem.*, 2002, **10**, 2283–2290.
72 R. Augusti, A. O. Dias, L. L. Rocha and R. M. Lago, *J. Phys. Chem. A*, 1998, **102**, 10723–10727.
73 K.-B. Cho, H. Hirao, S. Shaik and W. Nam, *Chem. Soc. Rev.*, 2016, **45**, 1197–1210.
74 J. C. Schöneboom, S. Cohen, H. Lin, S. Shaik and W. Thiel, *J. Am. Chem. Soc.*, 2004, **126**, 4017–4034.
75 S. N. Sharma, H. R. Sonawane and S. Dev, *Tetrahedron*, 1985, **41**, 2483–2491.
76 K. Honda, J. Cho, T. Matsumoto, J. Roh, H. Furutachi, T. Tosha, M. Kubo, S. Fujinami, T. Ogura, T. Kitagawa and M. Suzuki, *Angew. Chem., Int. Ed.*, 2009, **48**, 3304–3307.
77 Q.-F. Chen, K.-L. Xian, H.-T. Zhang, X.-J. Su, R.-Z. Liao and M.-T. Zhang, *Angew. Chem., Int. Ed.*, 2024, **63**, e202317514.